International Journal of Solids and Structures 135 (2018) 197–207

Contents lists available at ScienceDirect

International Journal of Solids and Structures

journal homepage: www.elsevier.com/locate/ijsolstr

Characterizing the nonlinear response of elastomeric material systems under critical point constraints

Shichao Cui, Ryan L. Harne*

Department of Mechanical and Aerospace Engineering, The Ohio State University, Columbus, OH 43210, USA

ARTICLE INFO

Article history:
Received 7 September 2017
Revised 16 November 2017
Available online 22 November 2017

ABSTRACT

Engineered materials that dissipate large shock and vibration through tailoring microscopic properties are of growing interest. To this end, reversible buckling of slender, elastomeric beams serving as microscopic constituents of engineered material systems is shown to be effective to tune the mechanical properties. Yet, the viscoelasticity and nonlinear deformations inherent in an engineered, elastomeric material system having critically constrained internal constituents challenge the understanding of the macroscopic dynamic properties borne out of such intersection of complex characteristics. This research undertakes analytical and experimental efforts considering a model specimen to illuminate how criticality, viscoelasticity, and nonlinearity interact to yield the macroscopic dynamic behavior of engineered, elastomeric material systems subjected to harmonic forcing. The analysis reveals that large strain of the internal beam constituents is a predominant mode of harmonic energy dissipation for more elastically dominated material characteristics. In contrast, a more equitable balance of viscous and elastic phenomena results in dissipation properties that involve history dependent reactions in tandem with the instantaneous strain on the constituents. Nonlinear deformations induced by critical constraints on the internal viscoelastic beams are discovered to strongly govern the relative amplitude of force transmission and significance of frequency tuning observed macroscopically. Experiments validate the findings and emphasize the non-intuitive character of elastomeric material system behaviors by virtue of the intersection of viscoelasticity, nonlinearity, and critical point constraints.

1. Introduction

Recent investigations on periodic cellular material systems have demonstrated the achievement of unprecedented macroscopic properties via sculpting or architecting internal geometries that are only observable at more microscopic length scales (Bertoldi, 2017). By leveraging elastomeric materials, instabilities ordinarily associated with structural failure, such as buckling, have been particularly cultivated as means to tailor mechanical properties, including stiffness, critical strain, and negative Poisson's ratio (Overvelde and Bertoldi, 2014; Shim et al., 2015; Babaee et al., 2013). The utility of these properties in dynamic loading conditions have shown that the elastic buckling behavior gives rise to wave propagation control and elastic energy trapping and release (Shan et al., 2015; Correa et al., 2015; Restrepo et al., 2015; Rudykh and Boyce, 2014). The latter phenomena have also been exploited at small scales using metallic and polymeric base materials in the material system fabrication (Meza et al., 2015; Frenzel et al., 2016; Torrents et al., 2012; Salari-Sharif et al., 2014). By harnessing the cellular geometries alongside elastic buckling in these new ways, the potential for lightweight and reusable shock absorbers and vibration isolators is empowered that contrast to prior conventions that rely on plastic deformation to mitigate vibration and wave energies.

The prevalence of elastomeric materials in the composition of such engineered material systems (Wang and Bertoldi, 2012) is encouraged by virtue of an inherent ability to dissipate shock and vibration via viscous damping influences (Rivin, 2003). The viscoelasticity of elastomers has been studied in great detail because of the significant diversity of contexts where elastomeric material systems are utilized (Lakes, 2009). Viscoelastic materials display viscous and elastic responses in consequence to applied stress and/or strain (Lakes, 2009), which results in delays between the phases of stress and strain when the materials are subjected to high-rate events. The influences of such delays on the dynamic response of linear viscoelastic materials is recognized to govern the onset of nonlinear deformations in elastomeric foams and magnetorheological elastomers (White et al., 2000; Singh et al., 2003; Li et al., 2010).

* Corresponding author.
E-mail address: harne.3@osu.edu (R.L. Harne).

https://doi.org/10.1016/j.ijsolstr.2017.11.020
0020-7683/

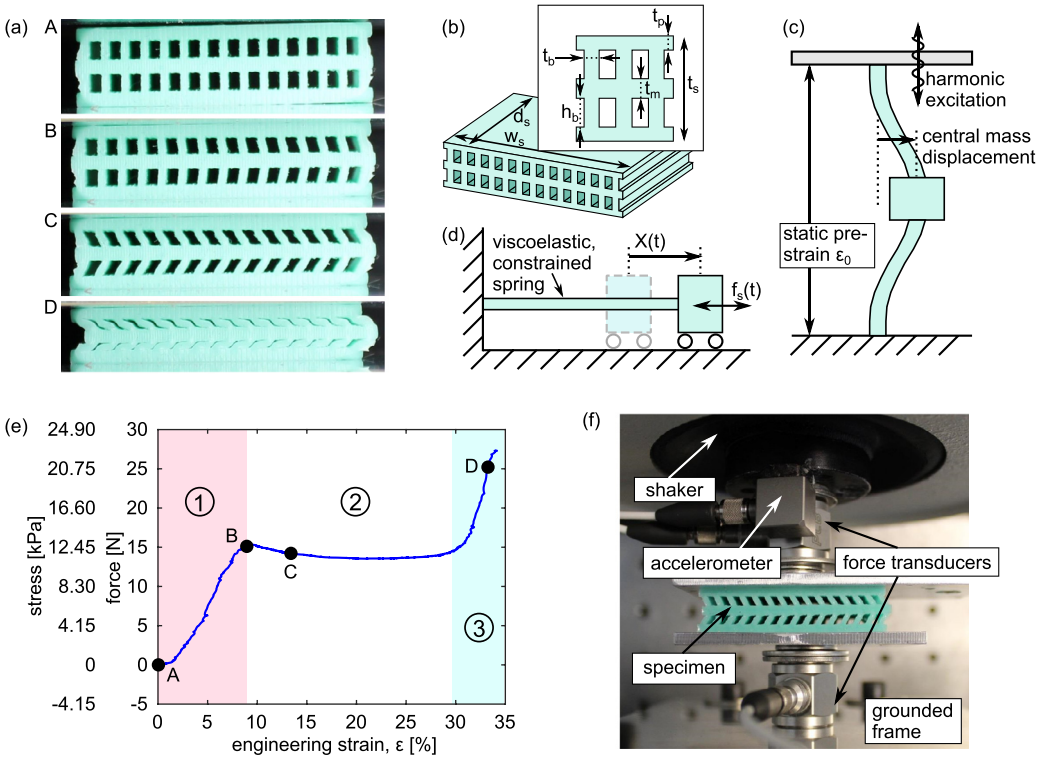

Fig. 1. (a) Cross section of the elastomeric material system, where labels (A, B, C, D) present the conditions when uncompressed, near the critical point, post-buckled, and post-buckled to an extent that compaction occurs. (b) Geometric conventions used to describe the material system topology. (c) Unit cell schematic. (d) A reduced order model schematic obtained from the unit cell. (e) Force-strain measurements of the system, where the corresponding labels (A, B, C, D) from (a) are shown to correspond to the loading condition. (f) Force transmissibility experimental setup.

Yet, for the aforementioned elastomeric materials that are mostly realized as a bulk, the deformation behavior through the material often varies linearly through the thickness. This contrasts with the deformation modes of engineered, elastomeric material systems with internal cellular geometries that may induce relatively large local translations, rotations, and shear motions having local strains far exceeding macroscopic strains (Bertoldi, 2017). Especially when instabilities are utilized that may magnify the local nonlinear deformations of internal microscale constituents (Bishop et al., 2016; Harne and Urbanek, 2017), such elastomeric material systems are a unique convergence of material and structural phenomena associated with viscoelasticity, critical constraints near instabilities, and large nonlinear deformations of internal geometries (Florijn et al., 2014). Although numerous efforts have assessed the decoupled influences of nonlinear deformations (Kidambi et al., 2016), linear viscoelasticity (Lakes, 2009), and constraints near instabilities observed in structural and material systems (Virgin and Wiebe, 2013; Cui and Harne, 2017), an analysis that elucidates their intersection has yet to be developed. Due to recent efforts that have revealed experimental and computational evidence of unique behaviors and dynamic properties cultivated under such conditions (Santer, 2010), including delayed snap-through in elastomeric shells when under sudden loads (Brinkmeyer et al., 2012), a clear need exists to establish a validated analytical framework to illuminate the dynamic properties of engineered, elastomeric material systems.

To begin meeting this broad need, this research undertakes complementary theoretical and experimental efforts that scrutinize the collective and coupled roles of nonlinearity, viscoelasticity, and criticality in elastomeric material systems subjected to harmonic loads. This report first describes the composition and fabrication of the elastomeric material system considered for closer study. Following a quantification of the mechanical properties, preliminary experimental results are given to exemplify the intricate coupling of the characteristics that warrant analytical assessment. Then, a new analytical model is formulated to characterize the material system constituent dynamic response induced by harmonic loads. Then, investigations are undertaken contrasting analytical and experimental findings in order to confidently conclude the respective influences of criticality, viscoelasticity, and nonlinearity on the material system behaviors. Concluding remarks are provided in the last section.

2. Elastomeric material system specimen composition and mechanical properties

The engineered, elastomeric material system considered in this report is shown in Fig. 1(a) part (A). The geometric conventions are denoted in Fig. 1(b). The material system cross-section geometry is reminiscent of the portal frame observed in structural sciences (Bažant and Cedolin, 2010), whereby stiff horizontally oriented members guide the motion of vertically oriented members. The internal geometry of the material system is composed of slender vertical beams with thickness $t_b = 1.08$ mm and height $h_b = 2.93$ mm that are connected through a central horizontal beam that guides lateral motion of the material system when under compressive load. The center horizontal beam thickness is $t_m = 2.11$ mm, which is sufficiently thick so that it displaces unilaterally under static and dynamic loads. Top and bottom horizontal elastomer beams are used for sake of realizing a more monolithic material system. The top and bottom horizontal beam thicknesses are both approximately $t_p = 2.05$ mm. The material system depth, macroscopic thickness, width, and mass are, respectively, $d_s = 26.87$ mm, $t_s = 12.14$ mm, $w_s = 44.85$ mm, and 11 g. These geometric features are selected to induce global post-buckling response of the material system when under static and dynamic loads. This is in

contrast to more localized post-buckling behaviors that would be observed should the vertical beam thicknesses be closer in proportion to the thicknesses of the several horizontal beams (Bažant and Cedolin, 2010).

Several steps are involved in the specimen fabrication. First, a 3D printer (FlashForge Creator Pro) is used to print a negative of the material system that serves as a mold. Then, silicone rubber (Smooth-on, Inc., Mold Star 15S) is poured into the mold and cured at room temperature. After a curing time of at least 8 hours, the specimen is removed from the mold and is ready to be carried into experiments after cleaning. Bulk silicone rubber fabricated by this process yields the mechanical properties of Young's modulus 318 kPa in compression, density 1145 kg/m, Poisson's ratio 0.499, and mild viscoelastic loss (see Appendix).

To examine the mechanical properties of the material system specimen, load frame experiments are carried out (Mark-10 ES20 frame, PCB 1102-05A load cell, Micro-Epsilon ILD 1700-200 laser displacement sensor). The specimen is positioned between a base plate and a top plate, where the latter is connected to the load cell. At least 4 loading cycles are undertaken to exercise the system and minimize the Mullin's effect for viscoelastic materials before collecting data (Bergström and Boyce, 1998). The engineering strain rate for the load frame experiments is 2.7×10^{-3} 1/s which is sufficiently slow to avoid notable time-history dependence of the base viscoelastic material (Slesarenko and Rudykh, 2016).

This model specimen is prime to investigate with the aim of uncovering the roles of the material system characteristics. To justify this argument, the unit cell of the specimen is shown in Fig. 1(c). Once given a static engineering pre-strain ε_0, harmonic loads cause motion of the unit cell central mass in the horizontal/lateral direction. According to the pre-strain, the dynamic response of the central mass in the lateral direction is drastically tailored according to the same harmonic excitation amplitude. Namely, the pre-strains may induce one of several distinct deformation modes of the material system as seen in Fig. 1(a). Label (A) shows the unconstrained specimen in the geometry associated with quasi-linear elastic compression. This regime is shown in the measurements of applied uniaxial force and engineering strain in Fig. 1(e). For engineering strains on the order of 0 to 9%, the quasi-linear elastic deformation mode occurs as labeled by the region 1 in Fig. 1(e).

The transition from this deformation state to the subsequent regime labeled region 2 is associated with the elastic buckling bifurcation, labeled (B) in Fig. 1(a) and (e). Around strains of 9%, the lateral motion of the central horizontal mass becomes more evident for further increase in strain, while the local linear stiffness of the specimen becomes negative. The lateral motion continues to grow through region 2 in Fig. 2(e) while the applied strain ranges from around 9 to 29%, thus causing greater lateral motion of the central horizontal mass, seen by part (C) of Fig. 1(a). The local linear stiffness of the system when strain is 5% in region 1 is about 20 kN/m, which contrasts to the mean stiffness in region 2 that is almost 0 kN/m. With further increasing strain as marked by region 3 in Fig. 1(e), compaction of the elastomeric material system occurs due to self-contact. The resulting force increases more under the same increase in strain than that in region 1, which indicates that the macroscopic stiffness is greater in region 3 than 1. Specifically, when the strain is 32% in area 3, the stiffness of the system is 40 kN/m, which is twice the stiffness measured for 5% in area 1. Due to the large shearing of the vertical beams that is induced in regions 2 and 3, it is logical to anticipate that nonlinearity associated with the large vertical beam deformations (Hodges, 1984) plays a considerable role when the pre-strain ε_0 upon the specimen is around 9% or greater.

According to the deformation modes observed in the load frame experiments, the deformation of the unit cell schematically shown in Fig. 1(c) is representative of the full range of global material system behavior, considering only translation of the central lumped mass. Due to the symmetry of the unit cell, a reduced order constituent schematic may be realized by that shown in Fig. 1(d). The viscoelastic spring is tunable according to a constraint parameter, with similar effect as the pre-strain ε_0 upon the unit cell in Fig. 1(c). Clearly, the significant variation of linear stiffness observed by the local slopes of curves in the force-strain profile in Fig. 1(e) suggest that the dynamic properties of the material system may corresponding vary across a wide range of behaviors depending on the pre-strain and amplitude of harmonic excitation. The understanding of how such aspects couple to the inherent viscoelasticity of the elastomeric beams in the material system requires careful analysis of the forced dynamic response.

3. Preliminary results of force transmission through the material system

For the purpose of characterizing the fundamental dynamic properties of the elastomeric material system under different pre-strain conditions, shaker experiments are conducted. As shown in Fig. 1(f), the experimental setup includes an electrodynamic shaker (LDS V408) that provides harmonic excitations to the specimen, an accelerometer (PCB 333B40) for control feedback to the vibration controller (Vibration Research VR9500), and force transducers on input (PCB 208C02) and output (PCB 208C01) sides of the specimen to quantify the harmonic force transmitted through the material system. The specimen is constrained between two aluminum plates connected to the input and output force transducers. Pre-strains are applied to the specimen by adjusting the fore/aft position of the shaker. A sinusoidal frequency sweep is carried out at a rate of 12 Hz/min, while data is collected at a sampling frequency 8192 Hz. The dimensionless force transmissibility transfer functions of output to input force are calculated from the frequency responses of the measurements.

The preliminary force transmissibility measurements are shown in Fig. 2. In each case, results are shown in a frequency band that fully encompasses the lowest order resonance identified. This resonant behavior is associated with greater, unilateral motion of the horizontal mass in the left/right directions according to the unit cell schematic of Fig. 1(c). Fig. 2(a) presents the results obtained with the material system in a pre-buckled condition using pre-strain $\varepsilon_0 = 4.2\%$. Results are obtained using different dynamic strain amplitude excitation amplitudes ε_d. When the dynamic strain amplitude increases, the force transmissibility peak shifts to 2% higher frequency with a 1% higher magnitude. In Fig. 2(b), the measurements are obtained for when the material system is near the critical point of buckling $\varepsilon_0 = 9.5\%$. When the amplitude of the dynamic strain increases around this critical regime, the force transmissibility amplitude decreases by 4% while the resonant frequency is unchanged at around 83 Hz. For a post-buckled condition of the system with $\varepsilon_0 = 31.8\%$, the results are shown in Fig. 2(c). From dynamic strain amplitude increases of 0.35%–0.74%, there is a 26% decrease in force transmissibility peak amplitude. With further increase in dynamic strain amplitude to 0.99% as presented by the blue dotted curve in Fig. 2(c), the force transmissibility amplitude is 449% percent of the amplitude that corresponds to 0.090 mm excitation amplitude. The significant increase in force transmissibility from the green dashed curve to the blue dotted curve is due to an onset of compaction in a dynamic manner.

Fig. 2(d) consolidates the force transmissibility measurements of the pre-buckled, near critical, and post-buckled conditions of the material systems when acted upon by the lowest amplitude dynamic strains considered, which are the red solid curves in Fig. 2(a)–(c). As shown in Fig. 2(d), the resonance amplitude decreases by 42% from pre-buckled to near-critical states induced by

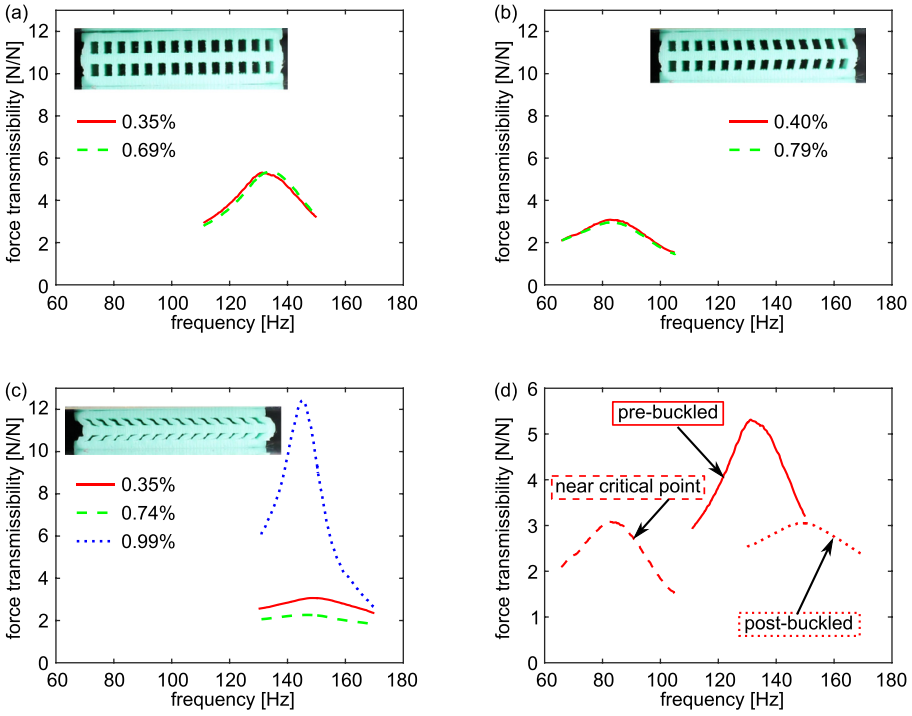

Fig. 2. Force transmissibility experimental results that vary the extent of pre-strain around the critical point of buckling. (a) Pre-buckled ($\varepsilon_0 = 4.2\%$), (b) near critical ($\varepsilon_0 = 9.5\%$), and (c) post-buckled ($\varepsilon_0 = 31.8\%$). The corresponding dynamic strain amplitude ε_d for each experiment is specified in the legends. (d) Consolidated results to compare force transmissibility of pre-buckled (solid curve), near critical point (dashed curve), and post-buckled (dotted curve) conditions with low dynamic strain amplitude. These are the red solid curves from (a,b,c).(For interpretation of the references to color in this figure legend, the reader is referred to the web version of this article.)

the pre-strain, while the resonance frequency shifts downward by 38%. Then with change of the pre-strain from near to criticality to the post-buckled condition, the peak output force amplitudes are almost unchanged. As a result, as the elastomeric material system is pre-strained in the regimes denoted as 1, 2, and 3 in Fig. 1(e), the resonance frequency first shifts to lower frequency and then shifts to higher frequency. Notably, the resonance frequency of the post-buckled dynamic response is nearly twice of the resonance frequency observed for the near critical point case, and also 15% higher than the pre-buckled dynamic response.

Surveying the works reported in Section 1, it is concluded that none of these intricate influences of the pre-strain or input force excitation amplitude upon the transmitted force response is alone explained by the large nonlinear deformations, manifestation of linear viscoelasticity, or nearness to criticality realized in the material system. Indeed, clearly an intersection of these material system characteristics must be the origin for such unusual tailoring of the force transmitted through the specimen when subjected to different operating conditions. Consequently, it is needed to devise an insightful analytical modeling approach able to probe these influences of viscoelasticity, criticality, and nonlinearity on the overall material system dynamic behavior.

4. Analytical modeling of the elastomeric material system

As found in Section 2, the reduced order schematic of the material system unit cell may be qualitatively realized by a lumped mass acted upon by a harmonic force and restored to an equilibrium via a constrained, viscoelastic spring. The mass motion is uniaxial, like the unilateral translation of the central horizontal beam of the material system specimen observed in Fig. 1(a). The goals of the analytical framework devised here are to first quantify the similarities of dynamic response between the reduced order constituent schematic and the whole material system as measured in the laboratory. Then, once validation is achieved, the analysis will become a vehicle for more in-depth study than that made feasible through exhaustive experimentation.

To compose the unit cell model, the appropriate terms that make up restoring forces returning the lumped mass to equilibrium are first identified. The pre-strain on the unit cell, Fig. 1(c), and resulting large local strains of the vertical beams that support the central horizontal mass encourage the adoption of constraint and nonlinearity parameters in the current analytical formulation that are established for nonlinear structural mechanics of beams loaded in their long axis (Virgin, 2007). To accommodate the linear viscoelastic material behaviors of the spring in the reduced order unit cell model, the model here builds from prior methods (Franceschini and Flori, 2001; Fosdick et al., 1998; Awrejcewicz and Dzyubak, 2006) to expand the space of states required to characterize the dynamic behavior. Thus, a new state associated with the memory of the viscoelastic material response is defined. The restoring force contribution of the history dependent viscoelastic material is introduced based on the standard linear solid model developed by Fosdick et al. (1998).

Once these model components are included and non-dimensionalized, the harmonically forced response of the reduced order unit cell schematic is governed by the equations

$$\ddot{x} + \eta\dot{x} + (1-p)x + \beta x^3 - \Phi\zeta = F\cos\omega\tau \tag{1a}$$

$$\dot{\zeta} = -\frac{1}{\gamma\omega_0}\zeta - 2\dot{x} \tag{1b}$$

In (1), the non-dimensional displacement of the lumped mass is $x = X/l_c$, where X is the physical displacement of the generalized coordinate and l_c is a characteristic length, often selected to be an original beam thickness or length in practice (Bažant and Cedolin, 2010). The auxiliary state ζ is associated with the memory of recent strain that governs the instantaneous dynamic behavior via a certain contribution to the total restoring force in (1a). It

has been shown that the fundamental elements of (1a,b) are mathematically analogous to the state space of the standard linear solid model of a viscoelastic material (Fosdick et al., 1998). The term $1-p$ denotes the nearness to criticality, such that the load parameter p is the ratio of the applied axial load (tailored by the pre-strain $\varepsilon_0$in practice) and the Euler buckling load for the vertical beams (Virgin, 2007). Because the linear stiffness vanishes at criticality, an accommodation to large, nonlinear deformations of the vertical beams is made via the coefficient β that defines the contribution of nonlinear beam bending curvature with respect to that obtained by a linear analysis (Hodges, 1984). The ratio of relaxation modulus to linear elastic spring stiffness is Φ. A viscous dashpot damping loss factor η is included due to observations that introduction of small, purely viscous damping greatly improves the agreement between experimental and analytical results for the material specimen studied here. The viscoelastic material relaxation time is γ while a non-dimensional time is introduction via $\tau=\omega_0 t$ in relation to the linear natural period of the unit cell oscillation $2\pi/\omega_0$. The non-dimensional frequency of the harmonic force excitation is $\omega=\Omega/\omega_0$, where Ω is the absolute excitation frequency and ω_0 is the linear elastic natural frequency of oscillation. Finally, the amplitude of the non-dimensional input force is F, while the overdot operator indicates $d/d\tau$.

The harmonic balance method (Harne and Wang, 2017) is utilized to approximately solve for the forced response of the material system unit cell. Assuming that the responses x and ζ occur at the same non-dimensional frequency as the harmonic force excitation, solutions to (1) are made via low order Fourier series expansions

$$x(\tau)=c(\tau)+a(\tau)\sin\omega\tau+b(\tau)\cos\omega\tau \tag{2a}$$

$$\zeta(\tau)=m(\tau)\sin\omega\tau+n(\tau)\cos\omega\tau \tag{2b}$$

where the coefficients c, a, b, m, and n are time-dependent. Then, (2) is substituted in to (1). The coefficients are considered to vary slowly in non-dimensional time such that dynamic contributions from second order derivatives are negligible. In addition, the higher order harmonics generated by the substitution are neglected since only the fundamental harmonic is assumed to contribute to the response under the single frequency of forced excitation. After substitution of (2) into (1), the coefficients of constant, sine, and cosine terms are collected together so as to yield a set of equations associated with the term types. Then, one obtains five unique algebraic equations with slow-varying coefficients

$$-\eta c'=\left(1-p+\frac{3}{2}\beta r^2+\beta c^2\right)c \tag{3a}$$

$$-\eta a'+2\omega b'=\Lambda a-\eta\omega b-\Phi m \tag{3b}$$

$$F-2\omega a'-\eta b'=\eta\omega a+\Lambda b-\Phi n \tag{3c}$$

$$-2a'-m'=-2\omega b+\sigma m-\omega n \tag{3d}$$

$$-2b'-n'=2\omega a+\omega m+\sigma n \tag{3e}$$

where

$$r^2=a^2+b^2 \tag{4}$$

$$\sigma=\frac{1}{\gamma\omega_0} \tag{5}$$

$$\Lambda=1-p-\omega^2+\frac{3}{4}\beta r^2+3\beta c^2 \tag{6}$$

Here r is the non-dimensional displacement amplitude of the material system constituent, and σ is the time constant ratio which is a ratio of natural oscillation period to the relaxation time of the underlying viscoelastic material. The (3) is also expressed

$$\mathbf{P}q'=G(q) \tag{7}$$

where $q=[c,\ a,\ b,\ m,\ n]^T$ is the vector of coefficients. The steady-state response is determined by solving (3) under the assumption of stationarity of coefficients. To this end, two third order polynomials are obtained in terms of the squared displacement amplitude r^2. One polynomial corresponds to the case $c^2=0$ which implies symmetric deformations of the unit cell around the equilibrium $x^*=0$,

$$\frac{9}{16}\beta^2 r^6+\left(\frac{3}{2}\beta(1-p+(\kappa\Phi-\omega)\omega)\right)r^4 +\left((\eta\omega+\kappa\sigma\Phi)^2+(1-p+(\kappa\Phi-\omega)\omega)^2\right)r^2-F^2=0 \tag{8}$$

The other polynomial corresponds to $c^2\neq 0$, in which case the deformations occur around the equilibrium $x^*=\sqrt{(p-1)/\beta}$,

$$\frac{225}{16}\beta^2 r^6+\left(\frac{15}{2}\beta(2(1-p)+(-\kappa\Phi+\omega)\omega)\right)r^4 +\left((\eta\omega+\kappa\sigma\Phi)^2+(2(1-p)+(-\kappa\Phi+\omega)\omega)^2\right)r^2-F^2=0 \tag{9}$$

Only positive real roots r determined from solving (8) and (9) are meaningful, while the dynamic stability of the periodic oscillation is assessed according to the eigenvalues of the Jacobian

$$\mathbf{J}=\left.\frac{d\left(\mathbf{P}^{-1}G\right)}{dq}\right|_{q=q^*} \tag{10}$$

Here, q^* is a set of coefficients that solves (3) under stationary conditions. Eigenvalues of (10) that have negative real components indicate that the roots are stable, whereas eigenvalues having positive real components correspond to unstable solutions (Harne and Wang, 2017). Unstable solutions to (3) are mathematically meaningful but are not physically realizable dynamic responses observed in experiments.

The non-dimensional transfer function of response amplitude to excitation force amplitude, termed receptance, is computed by

$$T_x=\frac{r}{F} \tag{11}$$

To compute the transfer function of output to input force amplitudes, termed force transmissibility, the output force expression is determined from (1a) as

$$F_r=\eta\dot{x}+(1-p)x+\beta x^3-\Phi\zeta \tag{12}$$

Substituting the assumed solution (2) into (12), the steady-state amplitude of the output force is found to be

$$F_r=\left[\left((1-p)a-\eta\omega b+\frac{3}{4}\beta a^3+\frac{3}{4}\beta ab^2+3\beta ac^2-\Phi m\right)^2 +\left(\eta\omega a+(1-p)b+\frac{3}{4}\beta a^2 b+\frac{3}{4}\beta b^3+3\beta bc^2-\Phi n\right)^2\right]^{1/2} \tag{13}$$

The non-dimensional force transmissibility is subsequently computed from

$$T_F=\frac{F_r}{F} \tag{14}$$

5. Preliminary assessment of analytical and experimental results

The efficacy of the analytical approach to predict the material system constituent dynamic response is examined with respect to

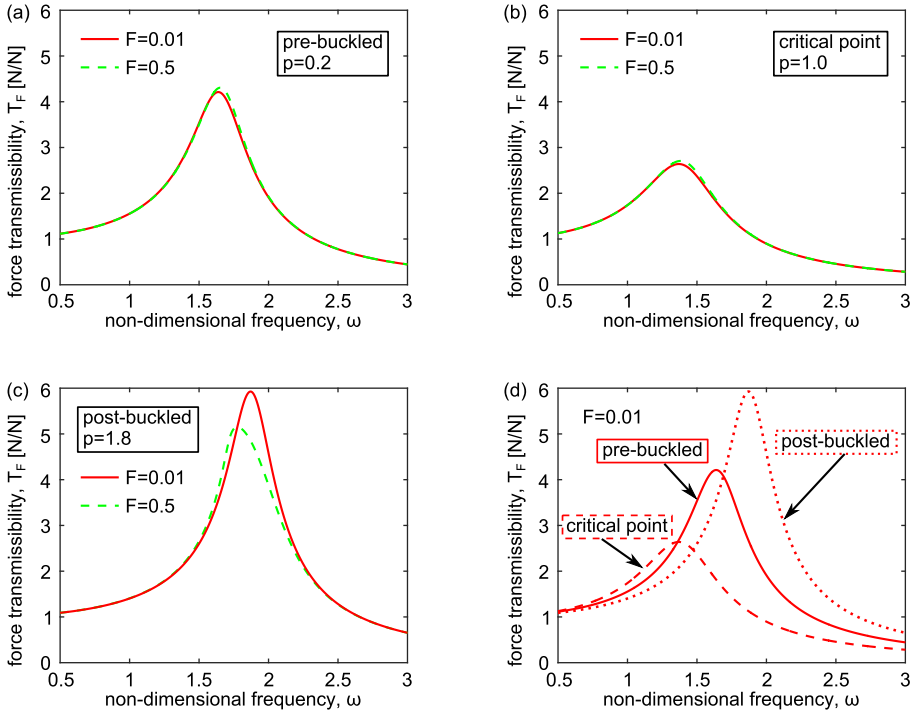

Fig. 3. Analytical force transmissibility results for (a) pre-buckled condition $p = 0.2$, (b) critical point constraint $p = 1.0$, and (c) post-buckled condition $p = 1.8$. Results for a low excitation amplitude $F = 0.01$ are indicated by red solid curves, and for a high excitation amplitude $F = 0.5$ are indicated by blue dashed curves. (d) Consolidated low excitation amplitude ($F = 0.01$) results. Solid curve represents pre-buckled condition, dashed curve represents critical point condition, and dash-dotted curve represents post-buckled condition. Additional parameters used in analysis are $(\omega_0, \eta, \beta, \Phi, \sigma) = (1, 0.05, 0.1, 1, 0.5)$.(For interpretation of the references to color in this figure legend, the reader is referred to the web version of this article.)

the preliminary experimental findings reported in Fig. 2. The qualitative agreement between the theoretical predictions and laboratory measurements is first sought for sake of projecting the utility of the analysis to investigate the complex interactions among the material viscoelasticity, the large nonlinear vertical beam deformations when subjected to constraints, and the relative nearness to criticality via the constraint.

Fig. 3 presents the analytical results of force transmissibility for different selections of the load parameter that denote nearness to criticality. Parameters used to obtain the analytical results are provided in the figure caption. In Fig. 3(a) the $p = 0.2$ the material system is pre-buckled. For an increase in the non-dimensional amplitude of force excitation from 0.01 (red solid curve) to 0.5 (blue dashed curve), the trend that force transmissibility peak amplitude and frequency increase by about 3% agrees well with the experimental results shown in Fig. 2(a). In Fig. 3(b), the load parameter is $p = 1$ to denote a critical point constraint. The increase in excitation amplitude increases the force transmissibility amplitude by about 2.5%, which compares to the experimental trend of a 4% decrease. Although the shifts of the peak force transmission differ between the measurements and predictions, the overall relative variation is small, and within the range of experimental and fabrication error, such as the practical difficulty in configuring the specimen with a precise critical point constraint via shaker position adjustment. For the post-buckled results shown in Fig. 3(c) via computations with load parameter $p = 1.8$, the response amplitude is clearly decreased by 15% and the resonance frequency is shifted to lower frequency for the increase amplitude of the input force. This agrees with the trend of experimental results (from red solid to green dashed, before compaction occurs) indicated in Fig. 2(c). As observed both analytically and experimentally, the amplitude of the input force has greater influence on the force transmissibility for the post-buckled condition of the material system than for pre-buckled or critically constrained states.

In Fig. 3(d), the predictions of force transmissibility are consolidated for the cases shown in (a,b,c) using the lower amplitude of input force. As the labels indicate in Fig. 3(d), from the pre-buckled condition (solid) to the critically constrained state of the material system (dashed), the force transmissibility peak amplitude decreases by 38%, from 4.2 to 2.6, and the non-dimensional peak frequency of resonant response shifts downwards by 18%. These trends are in good qualitative agreement with measurements reported in Fig. 2(d). With the increase in compressive constraint to transition from the critical condition to a post-buckled configuration of the material system, the peak amplitude of force transmission increases by 2.3 times of the amplitude at the critical condition. The resonance frequency also increases by 38%. Compared with the pre-buckled condition of the material system, the post-buckled force transmissibility peak has 40% greater amplitude and 13% higher frequency. The experimental results shown in Fig. 2(d) agree with these analytical predictions according to the observed tuning of force transmissibility peak frequency by the constraint extent. Also in good agreement between analysis and experiment is the finding that the material system constrained nearest to the critical point exhibits the lowest resonant frequency. Yet although the analytical and experimental material system behavior is comparable for the pre-buckled condition and critical point, the contrast differs for the post-buckled condition. Specifically, in the experiments Fig. 2(d) the post-buckled amplitude of peak force transmissibility is not greater than the pre-buckled condition, which is predicted by the analytical model Fig. 3(d). Indeed, the origin of such discrepancy is uncovered in the undertaking of the following studies that explore the relative roles that viscoelasticity, nonlinearity, and criticality play in determining the dynamic response of the material system when subjected to harmonic input force. It is important to note that the experimental and analytical results are not directly comparable between Figs. 2 and 3, respectively, because the model employs a time scale that is normalized to a

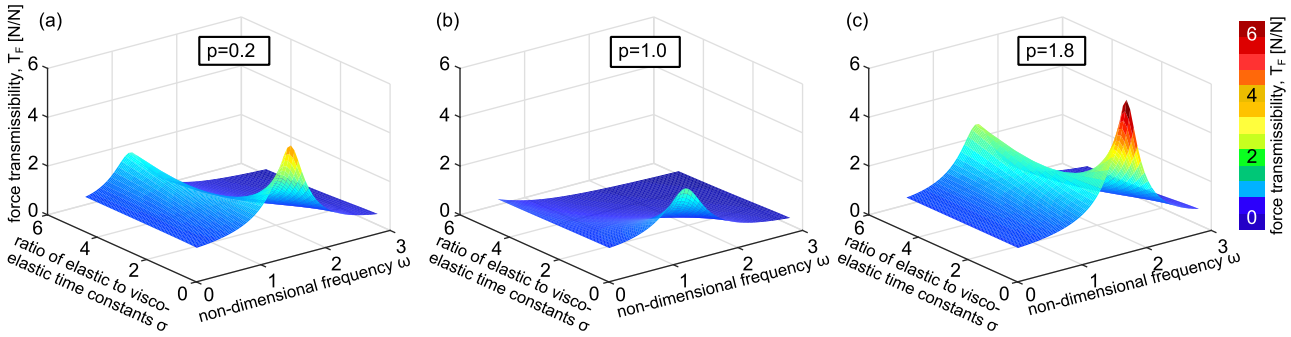

Fig. 4. Force transmissibility for (a) pre-buckled condition $p = 0.2$, (b) critical point $p = 1.0$, and (c) post-buckled condition $p = 1.8$. Parameters used for computation are (ω_0, η, β, Φ, F) = (1, 0.05, 0.1, 1, 0.01).

linear elastic natural frequency, which cannot be explicitly identified and decoupled from the frequency of free oscillation of the material system. On the other hand, an overall good qualitative agreement between analytical and experimental trends is observed in Figs. 2 and 3. As a result, a pathway is established to leverage the analysis to investigate the intricate and coupled roles of such material system characteristics on the dynamic behavior.

6. Studies on the intersections of criticality, viscoelasticity, and nonlinearity

In this section, the analytical approach to solve the non-dimensional equations (3) that govern the dynamic behavior of the material system unit cell is leveraged to explore the integrated influences of criticality, viscoelasticity, and nonlinearity. Although the fabrication capabilities used in this research are limited to modulate the relative significance of viscous compared to elastic behaviors of the material system by using material system geometric variation, emerging additive manufacturing techniques are demonstrating means to fabricate viscoelastic materials with large freedom over the material properties independent of geometric features (Hardin et al., 2015; Kokkinis et al., 2015). Moreover, the specific internal architecture of the material systems play significant roles in the resulting mechanical properties by virtue of the inherent integration of structural engineering principles with materials science in these emerging engineered media (Bertoldi, 2017; Shan et al., 2015). Consequently, the studies of this section uncover how the viscoelasticity, nonlinear deformations, and realizations of critical point constraints result in broad tuning of the force transmission through and dynamic response of the engineered, elastomeric material system shown in Fig. 1(a).

6.1. Assessments of weakly nonlinear dynamic behaviors of the harmonically forced viscoelastic and constrained material system unit cell

Previous efforts have shown quantitatively that certain material system internal architectures cultivate unusual macroscopic properties, such as extreme damping when global constraints give rise to critical point conditions for internal elements (Bishop et al., 2016; Lakes et al., 2001). In the model (3), the load parameter p governs the relative nearness of the unit cell to the critical point of buckling, with $p < 1$ being pre-buckled/critical, while constraints such that $p > 1$ imply post-buckled/critical states. To assess the influence of the load parameter alongside broad variation of the time constant ratio σ which expresses the ratio of elastic to viscous time constants, Fig. 4 presents analytical predictions of force transmissibility for (a) pre-buckled $p = 0.2$, (b) critical $p = 1.0$, and (c) post-buckled $p = 1.8$ conditions of the material system unit cell. The surface amplitude and color correspond to the force transmissibility as functions of the ratio σ and non-dimensional frequency of the harmonic input force ω. For the analytical results of Fig. 4, the relative significance of nonlinear deformations is low by selection of the parameter $\beta = 0.1$. Other parameters used to generate the analytical results are provided in the figure caption.

As shown in Fig. 4(a) for the pre-buckled condition $p = 0.2$, small or large values of the time constant ratio σ lead to relatively greater force transmissibility than for ratios σ spanning these extremes. Similar trends are observed for the post-buckled condition $p = 1.8$ shown in Fig. 4(c). Consequently, for these constrained conditions of the material system unit cell, an intermediate value of the time constant ratio may be identified that suppresses the force transmitted through the system, where these ratios are often around $\sigma = 2$ (in other words, the natural period of oscillation is twice the relaxation time). Comparatively, the critical point constraint $p = 1$ results shown in Fig. 4(b) reveal that a large overall reduction of the peak force transmission is achieved across the frequency bandwidth and range of time constant ratios. Specifically, the peak force transmissibility for $p = 1$ is reduced by 37% for $\sigma = 0.5$, and 60% for $\sigma = 5.0$ when compared to results for $p = 0.2$, and a corresponding reduction of 55% and 72% when compared to the results for $p = 1.8$. From these results, it may be concluded that at the critical point of buckling of the material system unit cell, force transmissibility is minimized when compared to the pre- and post-buckled conditions for viscoelastic materials. This conclusion is valid across a large range of time constant ratios σ. Moreover, these influences of criticality are greater when the material responds in a more elastic way, such that the time constant ratio is $\sigma > 1$. Namely, Fig. 4(b) shows more substantially reduced force transmission for $\sigma > 1$ than for $\sigma < 1$, which indicates that when the material properties are more strongly governed by elastic phenomena ($\sigma > 1$), the critical point constraint $p = 1.0$ gives rise to greater macroscopic damping mechanisms.

These influences are assessed in greater detail through Fig. 5 that presents analytical predictions of force transmissibility for three different time constant ratio σ values. For the case of time constant ratio $\sigma = 0.2$ shown in Fig. 5(a), as the load parameter p increases from 0 to 1, the frequency of peak force transmissibility lowers in value while the peak force transmissibility amplitude simultaneously decreases. As the load parameter p increases further from 1 to 2, the resonance frequency shifts to higher values at a faster rate for change in p than in the pre-buckled case. In addition, the peak amplitude of force transmissibility also increases to an extent that is greater than the pre-buckled condition. Similar trends are observed for time constant ratios $\sigma = 1$ in Fig. 5(b) and for $\sigma = 5$ in Fig. 5(c). Likewise, similar influences of the pre-strain ε_0 upon the force transmissibility measurements reported in Section 3 are uncovered.

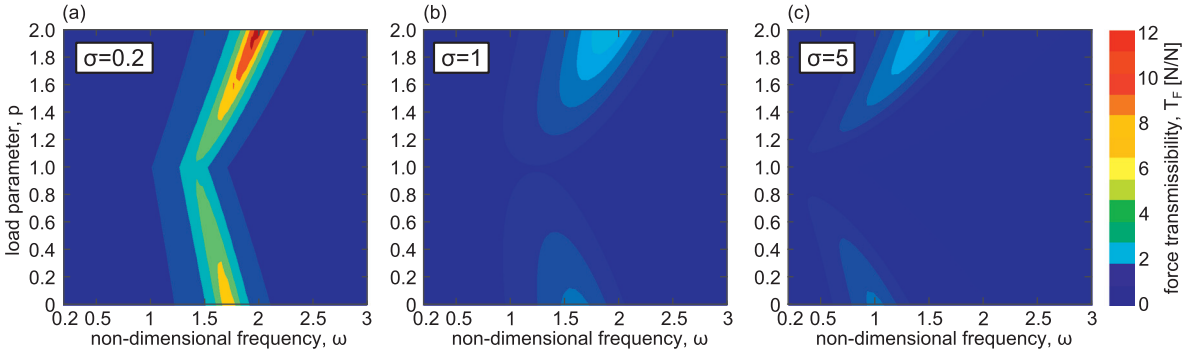

Fig. 5. Force transmissibility for ratios of natural period to relaxation time (a) $\sigma = 0.2$, (b) $\sigma = 1$, and (c) $\sigma = 5$. Parameters used for computation are $(\omega_0, \eta, \beta, \Phi, F) = (1, 0.05, 0.1, 1, 0.01)$.

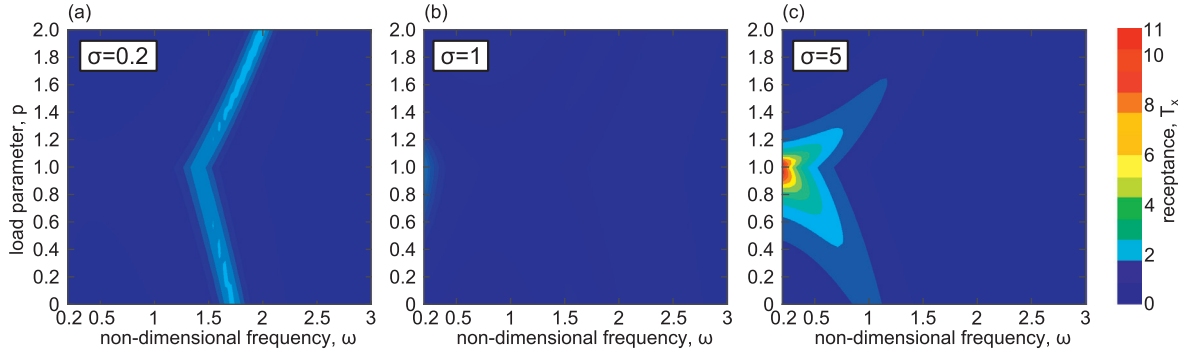

Fig. 6. Receptance contours for ratios of natural period to relaxation time (a) $\sigma = 0.2$, (b) $\sigma = 1$, and (c) $\sigma = 5$. Parameters used for computation are $(\omega_0, \eta, \beta, \Phi, F) = (1, 0.05, 0.1, 1, 0.01)$.

From the results of Fig. 5(a) and (b), the overall force transmissibility amplitudes for the material system with time constant ratio $\sigma = 1$ are uniformly smaller than that of $\sigma = 0.2$, although the frequency band around which peak force transmission occurs is not significantly different. This contrasts with the case of time constant ratio $\sigma = 5$ presented in Fig. 5(c) that reveals a more substantial reduction of frequency to small values near $\omega = 0$ as the load parameter tends to $p = 1$. For this greater proportion of elastic phenomena contributing to the material system behavior with $\sigma = 5$, near the critical point $p = 1$ the force transmissibility is almost zero over the whole frequency range. Consequently, the collective results of Fig. 5 suggest that constraints near to the critical point $p = 1$ uniformly reduce transmitted force through the elastomeric material system, regardless of the relative proportion of viscous to elastic phenomena to govern the material system properties (at least within the range $0.2 < \sigma < 5$). This finding explicitly supports observations made previously in examinations of critically constrained engineered metamaterials in impact/drop experiments (Bishop et al., 2016) and agree with related analytical predictions using linearized models (Antoniadis et al., 2015; Kochmann, 2014).

The explanation for the reduction of dynamic force transmitted through the material system unit cell is elucidated by studying the receptance contours in Fig. 6 that are generated using the same parameters are those employed in Fig. 5. As a ratio of the internal displacement amplitude to the harmonic input force, the receptance quantifies the internal deformation induced by the excitation. The results of Fig. 6 reveal that the receptance is maximized near the critical point when $\sigma \geq 1$, whereas the internal displacement motion is greater for higher or lower values of the load parameter when viscous phenomena predominate the material properties, such that $\sigma < 1$. Interestingly, the peak of receptance for the case of time constant ratio $\sigma = 1$ is the lowest among the three cases shown. This indicates that the absolute amplitude of the internal material system constituent oscillation is least when the material composition equally balances viscous and elastic characteristics. Coupled to the low transmission of force as observed in Fig. 5(b), the use of such a "balanced" viscoelastic material induces notable tailoring of the force transmission properties as well as minimizes the internal strains acting upon the unit cell, which are the vertical beams in bending and shearing, Fig. 1(a) and (c). These are practical insights that may motivate concepts for resilient vibration isolators or shock attenuators.

In Fig. 6(c), it is found that the receptance amplitude is large for low frequency near the critical point. The least force transmission is observed in this same parameter regime in Fig. 5(c). This establishes the explanation that force transmission is minimized for the more elastic material system composition ($\sigma = 5$) when the internal constituents are most strained due to large deformation (large receptance). This establishes a theoretical supporting basis to prior hypotheses that the primary energy dissipation mechanism in critically constrained engineered material systems composed of elastic media is due to large internal strains of the constrained members (Antoniadis et al., 2015). Of course, for damped, elastic resonant metamaterials, this is the primary mode of energy attenuation (Hussein and Frazier, 2013). Interestingly, this contradicts the observed trends for the material system unit cell results with more viscous dominated behaviors, $\sigma < 1$, like that shown in Fig. 6(a) where the receptance is not maximized at a parametric point coincident with minimum force transmission in Fig. 5(a).

6.2. Influences of greater nonlinear deformations on the unit cell material behavior

The analytical results presented in Figs. 3–6 considered a relatively small contribution of nonlinear bending and stretching via use of parameter $\beta = 0.1$. On the other hand, the near-critical con-

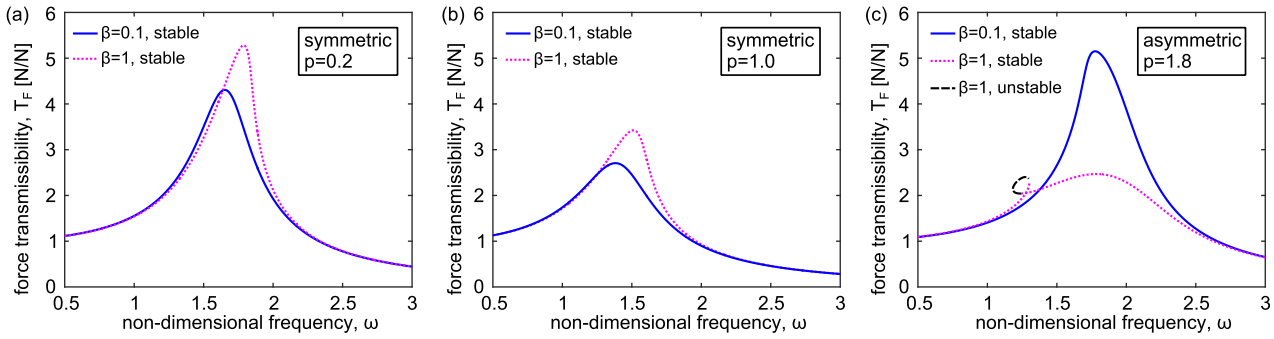

Fig. 7. Force transmissibility for (a) pre-buckled $p = 0.2$, (b) critical point $p = 1.0$, and (c) post-buckled $p = 1.8$ conditions. Comparison is made between a relatively low contribution from nonlinear deformations $\beta = 0.1$ (blue solid curves) and higher contribution $\beta = 1$ (magenta dotted curves). Parameters used for computation are (ω_0, η, σ, Φ, F) = (1, 0.05, 0.5, 1, 0.5).(For interpretation of the references to color in this figure legend, the reader is referred to the web version of this article.)

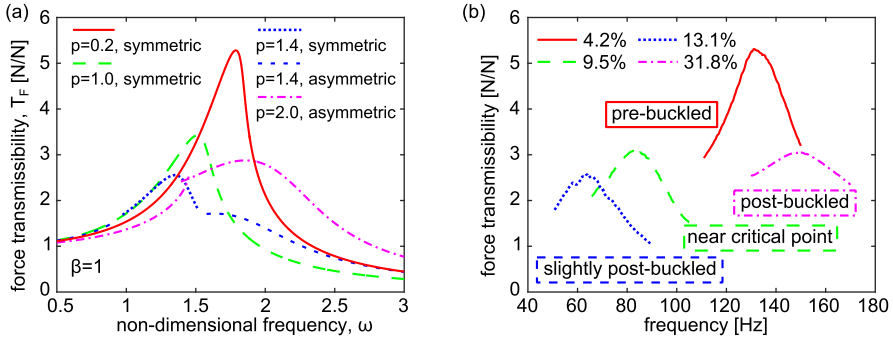

Fig. 8. (a) Analytical results of force transmissibility using load parameters p at and variably below and beyond the critical point of $p = 1$. Parameters used for computation are (ω_0, η, σ, Φ, F) = (1, 0.05, 0.5, 1, 0.5). (b) Experimental results of force transmissibility of below, near to, and beyond the critical point by variation of the pre-strain, which are indicated in the legends.

straints suggest that the large deformations of the internal vertical viscoelastic beams of the material system, Fig. 1(a), may be exacerbated when subjected to harmonic input force because the linear elastic restoring forces are eliminated for cases around $p = 1$ (Virgin, 2007). Thus, here the influence of the relative contribution of nonlinear bending and stretching is examined for its influence on the material system dynamic behavior in tandem with the roles of viscoelasticity and criticality.

Fig. 7 presents the analytical force transmissibility results of (a) pre-buckled $p = 0.2$, (b) critical point $p = 1.0$, and (c) post-buckled of $p = 1.8$ conditions of the material system when the time constant ratio $\sigma = 0.5$, indicating that the relaxation time is twice the natural period of oscillation. In each subfigure, blue solid curves represent results obtained using $\beta = 0.1$, while magenta dotted curves denote that $\beta = 1$. For conditions of $p = 0.2$ and $p = 1.0$, as shown in Fig. 7(a) and (b) respectively, the larger β leads to 23% and 26% increase in force transmissibility amplitude. For these cases of load parameter $p \leq 1$, the responses of the material system constituent are symmetric stable responses that oscillate around zero equilibrium $x^* = 0$. For the post-buckled material system such that a pre-strain leads to $p = 1.8$, Fig. 7(c), a more significant contribution from nonlinear deformations by $\beta = 1$ results in decreased force transmissibility amplitude by 52% when compared to $\beta = 0.1$. When the unit cell is post-buckled, the stable responses are asymmetric around the equilibrium $x^* = 2.83$ for $\beta = 0.1$, and $x^* = 0.89$ for $\beta = 1$, while the unstable (non-physical) predictions of force transmissibility are shown in Fig. 7(c) for sake of completeness. The nonlinearity has an effect on the force transmissibility amplitude that cannot be neglected, and the influence regarding the trend of increasing or decreasing the amplitude is different for $p \leq 1$ and $p > 1$. From the analytical results presented in prior sections of this report, the force transmissibility amplitudes at the critical points are the lowest compared with pre- and post-buckled conditions. Yet here, it is noticed when comparing the results of force transmissibility of $\beta = 1$ for different buckling conditions (magenta dotted curves in Fig. 7), the peak amplitude for the post-buckled condition in Fig. 7(c) with $p = 1.8$ is lower than that peak observed when the material system is loaded at the critical point, Fig. 7(b).

Indeed, this feature is in qualitative agreement with the observation from the preliminary experimental results in Fig. 2(d) that suggested a discrepancy with the preliminary analytical predictions in Fig. 3(d). In other words, the significance of nonlinear deformations on tailoring the force transmission measured experimentally may have been greater than that anticipated via the use of $\beta = 0.1$ to generate Fig. 3(d). To look into this feature in greater detail, the nuanced roles of the load parameter p when $\beta = 1$ and $\sigma = 0.5$ are given in Fig. 8.

Fig. 8(a) shows that the frequency of peak force transmissibility and the peak amplitude both decrease when the pre-strain is changed such that is goes from critical $p = 1$ to just beyond critical so that $p = 1.4$. As the pre-strain on the material system unit cell is made greater to shift from $p = 1.4$ to $p = 2.0$, the force transmissibility peak frequency and amplitude increase. Yet the peak of force transmissibility when $p = 2.0$ is still smaller than that at the critical point $p = 1.0$, and also much smaller than that at the pre-buckled point $p = 0.2$. For $\beta = 0.1$ as shown in Fig. 5, the critical point $p = 1.0$ coincides with the least force transmissibility peak amplitude for all cases of the load parameter p and time constant ratio σ. On the other hand, the increase in the significance of nonlinear deformations by $\beta = 1$ modulates this trend such that the force transmissibility peak amplitude and frequency are the least for load parameters $p > 1$. For $p = 1.4$ when $\beta = 1$ as presented in Fig. 8(a), symmetric and asymmetric stable responses may be induced, indicating that the unit cell may oscillate laterally back-and-

forth between the stable configurations (symmetric) or may oscillate around either of the post-buckled equilibria (asymmetric, one of which is shown in Fig. 1(a) part (C)).

To experimentally validate these analytical findings and close the loop on the prior discrepancy between analysis and experiment, additional experiments are conducted with the results presented in Fig. 8(b). Here, the pre-strain is tailored from the pre-buckled point $\varepsilon_0 = 4.2\%$, to the critical point $\varepsilon_0 = 9.5\%$ (red solid curve), to slightly post-buckled $\varepsilon_0 = 13.1\%$ (blue dashed curve), to still further post-buckled $\varepsilon_0 = 31.8\%$ (magenta dash-dot curve). These pre-strains may be identified in Fig. 1(e) with respect to the corresponding significance of deformation of the material system specimen using the photographs and labels in Fig. 1. As Fig. 8(b) indicates, from near the critical point to a slightly post-buckled condition, both the peak frequency and amplitude of force transmissibility decrease. This agrees qualitatively with the respective analytical predictions for $p = 1$ and $p = 1.4$ in Fig. 8(a). From the slightly post-buckled to a more post-buckled condition, the peak frequency increases from around 65 Hz to 150 Hz, and the peak amplitude increases by 18%, although it is similar to that peak of force transmissibility measured for the near critically constrained material system. These experimental findings also agree well with the analytical predictions in Fig. 8(a). Therefore, the significance of nonlinear deformations of the vertical beams in the engineered, elastomeric material system explains why the force transmissibility amplitude of the post-buckled state is not greater than that observed for the near critical or pre-buckled conditions in Fig. 2(d).

7. Conclusions

The accelerated interest to architect elastomeric materials that possess cellular, internal geometries for tailoring vibration and elastic wave propagation behaviors has introduced a need to elucidate the intricate and coupled influences of viscoelasticity, nonlinear deformations, and critical point constraints on the dynamics of the engineered material systems. This research establishes an analytical approach to uncover the intertwined relationships among such material system characteristics and validates the efficacy of the predictions via agreement with experiments. By tuning the unit cell of the material system to be near the critical point of buckling, the force transmissibility peak frequency and amplitude are minimized when the contribution of nonlinear deformations β is low. For the time constant ratios $\sigma \geq 1$ that correspond to more elastically dominated material behavior, this reduction of force transmissibility is associated with large internal strain of the material system constituent, namely the vertical beam bending and shearing observed experimentally. On the other hand, the analytical predictions suggest that for material systems fabricated such that the viscous nature of the elastomeric materials predominates, $\sigma < 1$, the history dependent nature of the viscoelastic material is coupled with the large deformations of the material system constituent such that the force transmissibility reduction is not coincident with peak receptance and strain. Moreover, for a material system with more significant contribution from nonlinear deformations in the pre-strained vertical beams, the peak force transmissibility frequency and amplitude may be minimized when the pre-strain is slightly beyond critical, in contrast to the exact critical point itself. These trends are borne out in the experiments and provide strong qualitative agreement with the analytical predictions. In summary, this research reveals the integrated influence of criticality, viscoelasticity, and nonlinearity on the dynamic properties of an elastomeric material system, and exemplifies that such intertwined characteristics cannot be neglected in the assessment of high-rate oscillations induced by forced excitations.

Acknowledgment

This work is supported in part by the Ford Motor Company.

Appendix

The mechanical and dynamic properties of the base silicone rubber material (Smooth-on, Inc., Mold Star 15S) used for the experimental specimen are provided in Fig. 9. The measurements are conducted at room temperature in uniaxial compression. The silicone rubber material sample from which the data are derived is a cylinder of 8 mm diameter and 8 mm length. The density of the material is measured to be around 1145 kg/m^3. Fig. 9(a) shows the compressive stress measured by a load frame (Tinius Olsen H10KS) with 100 N load cell as uniaxial compressive strain is applied to the sample. The compressive Young's modulus is found to be around 318 kPa. To measure dynamic properties, a dynamic mechanical analysis (DMA) is conducted with dynamic strain amplitude of 50 μm (TA Instruments, Ares). The loss tangent, tan δ, measured from the sample is presented in Fig. 9(b). Resonant behavior is observed around 50 Hz. The tan δ increases in value below this resonant feature and greatly reduces above the resonance. In general, the DMA results demonstrate that the base silicone rubber material has mild viscoelastic loss, tan $\delta < 0.2$ outside of the narrow-band resonant frequency range. Such trends in tan δ are indicative of silicone rubbers modeled as standard linear solids (Shipkowitz et al., 1988). This data supports the model composition used in this research, presented in Section 4, that accounts for the viscoelasticity of the base material of the material system.

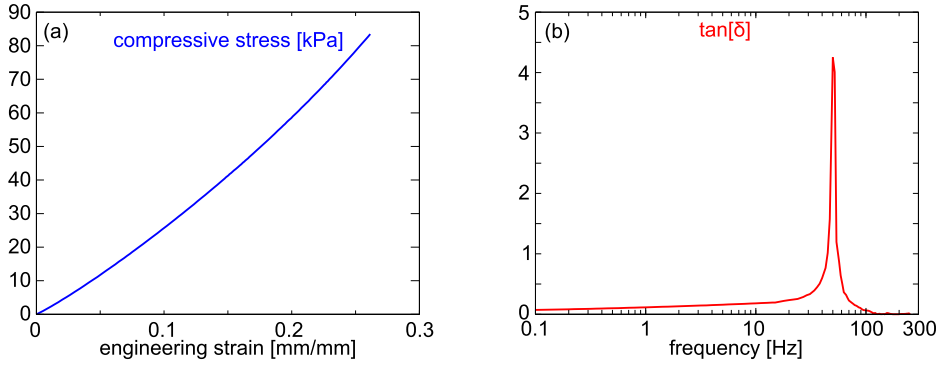

Fig. 9. Base material properties for compression of the silicone rubber used on the material system specimen studied in this research. (a) Mechanical properties in stress/strain. (b) tan δ measured from DMA.

References

Antoniadis, I., Chronopoulos, D., Spitas, V., Koulocheris, D., 2015. Hyper-damping peroperties of a stiff and stable linear oscillator with a negative stiffness element. J. Sound Vib. 346, 37–52.

Awrejcewicz, J., Dzyubak, L., 2006. Modeling, chaotic behavior, and control of dissipation properties of hysteretic systems. Math. Prob. Eng. 2006, 94929.

Babaee, S., Shim, J., Weaver, J.C., Chen, E.R., Patel, N., Bertoldi, K., 2013. 3D soft metamaterials with negative Poisson's ratio. Adv. Mater. 25, 5044–5049.

Bažant, Z.P., Cedolin, L., 2010. Stability of Structures: Elastic, Inelastic, Fracture, and Damage Theories. World Scientific Publishing Co.

Bergström, J.S., Boyce, M.C., 1998. Constitutive modeling of the large strain time-dependent behavior of elastomers. J. Mech. Phys. Solids 46, 931–954.

Bertoldi, K., 2017. Harnessing instabilities to design tunable architected cellular materials. Ann. Rev. Mater. Res. 47, 51–61.

Bishop, J., Dai, Q., Song, Y., Harne, R.L., 2016. Resilience to impact by extreme energy absorption in lightweight material inclusions constrained near a critical point. Adv. Eng. Mater. 18, 1871–1876.

Brinkmeyer, A., Santer, M., Pirrera, A., Weaver, P.M., 2012. Pseudo-bistable self-actuated domes for morphing applications. Int. J. Solids Struct. 40, 1077–1087.

Correa, D.M., Klatt, T., Cortes, S., Haberman, M., Kovar, D., Seepersad, C., 2015. Negative stiffness honeycombs for recoverable shock isolation. Rapid Prototyping J. 21, 193–200.

Cui, S., Harne, R.L., 2017. Tailoring broadband acoustic energy suppression characteristics of double porosity metamaterials with compression constraints and mass inclusions. J. Acoust. Soc. Am. 141, 4715–4726.

Florijn, B., Coulais, C., van Hecke, M., 2014. Programmable mechanical metamaterials. Phys. Rev. Lett. 113, 175503.

Fosdick, R., Ketema, Y., Yu, J.H., 1998. Vibration damping through the use of materials with memory. Int. J. Solids Struct. 35, 403–420.

Franceschini, G., Flori, R., 2001. Vibrations of a body supported by shear mountings of incompressible material with memory. Int. J. Eng. Sci. 39, 1013–1031.

Frenzel, T., Findeisen, C., Kadic, M., Gumbsch, P., Wegener, M., 2016. Tailored buckling microlattices as reusable light-weight shock absorbers. Adv. Mater. 28, 5865–5870.

Hardin, J.O., Ober, T.J., Valentine, A.D., Lewis, J.A., 2015. Microfluidic printheads for multimaterial 3d printing of viscoelastic inks. Adv. Mater. 27, 3279–3284.

Harne, R.L., Urbanek, D.C., 2017. Enhancing broadband vibration energy suppression using local buckling modes in constrained metamaterials. J. Vib. Acoust. 139, 061004.

Harne, R.L., Wang, K.W., 2017. Harnessing Bistable Structural Dynamics: For Vibration Control, Energy Harvesting and Sensing. John Wiley & Sons Ltd.

Hodges, D.H., 1984. Proper definition of curvature in nonlinear beam kinematics. AIAA Journal 22, 1825–1827.

Hussein, M.I., Frazier, M.J., 2013. Metadamping: an emergent phenomenon in dissipative metamaterials. J. Sound Vib. 332, 4767–4774.

Kidambi, N., Harne, R.L., Wang, K.W., 2016. Adaptation of energy dissipation in a mechanical metastable module excited near resonance. J. Vib. Acoust. 138, 011001.

Kochmann, D.M., 2014. Stable extreme damping in viscoelastic two-phase composites with non-positive-definite phases close to the loss of stability. Mech. Res. Commun. 58, 36–45.

Kokkinis, D., Schaffner, M., Studart, A.R., 2015. Multimaterial magnetically assisted 3d printing of composite materials. Nature Commun. 6, 8643.

Lakes, R., 2009. Viscoelastic Materials. Cambridge University Press.

Lakes, R.S., Lee, T., Bersie, A., Wang, Y.C., 2001. Extreme damping in composite materials with negative-stiffness inclusions. Nature 410, 565–567.

Li, W.H., Zhou, Y., Tian, T.F., 2010. Viscoelastic properties of MR elastomers under harmonic loading. Rheologica acta 49, 733–740.

Meza, L.R., Zelhofer, A.J., Clarke, N., Mateos, A.J., Kochmann, D.M., Greer, J.R., 2015. Resilient 3d hierarchical architected metamaterials. Proc. Natl. Acad. Sci. 112, 11502–11507.

Overvelde, J.T.B., Bertoldi, K., 2014. Relating pore shape to the non-linear response of periodic elastomeric structures. J. Mech. Phys. Solids 64, 351–366.

Restrepo, D., Mankame, N.D., Zavattieri, P.D., 2015. Phase transforming cellular materials. Extreme Mech. Lett. 4, 52–60.

Rivin, E.I., 2003. Passive Vibration Isolation. ASME Press.

Rudykh, S., Boyce, M.C., 2014. Transforming wave propagation in layered media via instability-induced interfacial wrinkling. Phys. Rev. Lett. 112, 034301.

Salari-Sharif, L., Schaedler, T.A., Valdevit, L., 2014. Energy dissipation mechanisms in hollow metallic microlattices. J. Mater. Res. 29, 1755–1770.

Santer, M., 2010. Self-actuated snap back of viscoelastic pulsing structures. Int. J. Solids Struct. 47, 3263–3271.

Shan, S., Kang, S.H., Raney, J.R., Wang, P., Fang, L., Candido, F., Lewis, J.A., Bertoldi, K., 2015. Multistable architected materials for trapping elastic strain energy. Adv. Mater. 27, 4296–4301.

Shim, J., Wang, P., Bertoldi, K., 2015. Harnessing instability-induced pattern transformation to design tunable phononic crystals. Int. J. Solids Struct. 58, 52–61.

Shipkowitz, A.T., Chen, C.P., Lakes, R.S., 1988. Characterization of high-loss viscoelastic elastomers. J. Mater. Sci. 23, 3660–3665.

Singh, R., Davies, P., Bajaj, A.K., 2003. Identification of nonlinear and viscoelastic properties of flexible polyurethane foam. Nonlinear Dyn. 34, 319–346.

Slesarenko, V., Rudykh, S., 2016. Harnessing viscoelasticity and instabilities for tuning wavy patterns in soft layered composites. Soft Matter 12, 3677–3682.

Torrents, A., Schaedler, T.A., Jacobsen, A.J., Carter, W.B., Valdevit, L., 2012. Characterization of nickel-based microlattice materials with structural hierarchy from the nanometer to the millimeter scale. Acta Materialia 60, 3511–3523.

Virgin, L.N., Wiebe, R., 2013. On damping in the vicinity of critical points. Philos. Trans. R. Soc. A 371, 20120426.

Virgin, L.N., 2007. Vibration of Axially Loaded Structures. Cambridge University Press.

Wang, L., Bertoldi, K., 2012. Mechanically tunable phononic band gaps in three-dimensional periodic elastomeric structures. Int. J. Solids Struct. 49, 2881–2885.

White, S.W., Kim, S.K., Bajaj, A.K., Davies, P., 2000. Experimental techniques and identification of nonlinear and viscoelastic properties of flexible polyurethane foam. Nonlinear Dynamics 22, 281–313.